Insight into Physical and Thermodynamic Properties of X_3Ir (X = Ti, V, Cr, Nb and Mo) Compounds Influenced by Refractory Elements: A First-Principles Calculation

Dong Chen [1,2,3], Jiwei Geng [1], Yi Wu [2], Mingliang Wang [1,*] and Cunjuan Xia [2,*]

[1]   State Key Laboratory of Metal Matrix Composites, Shanghai Jiao Tong University, No. 800 Dongchuan Road, Shanghai 200240, China; chend@sjtu.edu.cn (D.C.); gengjiwei163@sjtu.edu.cn (J.G.)

[2]   School of Materials Science & Engineering, Shanghai Jiao Tong University, No. 800 Dongchuan Road, Shanghai 200240, China; eagle51@sjtu.edu.cn

[3]   Anhui Province Engineering Research Center of Aluminium Matrix Composites, Huaibei 235000, China

*   Correspondence: mingliang_wang@sjtu.edu.cn (M.W.); xiacunjuan@sjtu.edu.cn (C.X.);
    Tel.: +86-21-34202540 (M.W. & C.X.)

check for
updates

Abstract: The effects of refractory metals on physical and thermodynamic properties of X_3Ir (X = Ti, V, Cr, Nb and Mo) compounds were investigated using local density approximation (LDA) and generalized gradient approximation (GGA) methods within the first-principles calculations based on density functional theory. The optimized lattice parameters were both in good compliance with the experimental parameters. The GGA method could achieve an improved structural optimization compared to the LDA method, and thus was utilized to predict the elastic, thermodynamic and electronic properties of X_3Ir (X = Ti, V, Cr, Nb and Mo) compounds. The calculated mechanical properties (i.e., elastic constants, elastic moduli and elastic anisotropic behaviors) were rationalized and discussed in these intermetallics. For instance, the derived bulk moduli exhibited the sequence of $Ti_3Ir < Nb_3Ir < V_3Ir < Cr_3Ir < Mo_3Ir$. This behavior was discussed in terms of the volume of unit cell and electron density. Furthermore, Debye temperatures were derived and were found to show good consistency with the experimental values, indicating the precision of our calculations. Finally, the electronic structures were analyzed to explain the ductile essences in the iridium compounds.

Keywords: Ir-based intermetallics; refractory metals; elastic properties; ab initio calculations

1. Introduction

Ir-based superalloys have received intensive interest in the last decades due to their high melting temperature as well as their improved strength, oxidation resistance and corrosion resistance at higher temperatures [1–5]. Consequently, these intermetallics can be deemed a suitable choice for high-temperature applications. For example, the cubic $L1_2$ intermetallic compounds Ir_3X (X = Ti, Zr, Hf, Nb and Ta) containing refractory elements could be proposed as "refractory superalloys" based on their higher melting points and superior mechanical properties at higher temperatures [3–5]. Terada et al. [6] conducted measurements on thermal properties (i.e., thermal conductivity and thermal expansion) from 300 to 1100 K, and found that the $L1_2$ Ir_3X (X = Ti, Zr, Hf, Nb and Ta) compounds were characterized by a larger thermal conductivity and a smaller thermal expansion. Chen et al. [7] exhibited the elastic constants and moduli of binary $L1_2$ Ir-based compounds at ground states by first-principles calculations, and reported the higher elastic moduli of these compounds together with their brittle characteristics in nature. Liu et al. [8] studied the elastic and thermodynamic properties of

Ir$_3$Nb and Ir$_3$V under varying pressure (0–50 GPa) and temperature (0–1200 K), and found that both compounds were stable without phase transformations.

Meanwhile, the typical refractory intermetallics should also include A15 cubic structure compounds with refractory metal elements. For example, Pan et al. [9] reported the mechanical and electronic properties of Nb$_3$Si using the first-principles method. By combining the first-principles method with quasi harmonic approximation, Papadimitriou et al. [10–12] critically investigated the mechanical and thermodynamic properties of Nb$_3$X (X = Al, Ge, Si and Sn). Chihi et al. [13] theoretically evaluated the elastic and thermodynamic properties of V$_3$X (X = Si, Ge and Sn) intermetallics utilizing the first-principles calculations. Jalborg et al. [14] determined the electronic structure of V$_3$Ir, V$_3$Pt and V$_3$Au using the self-consistent semi relativistic linear muffin-tin orbital (LMTO) band calculations. Paduani et al. [15] investigated the chemical bonding behavior and estimated the electron-phonon coupling constants of V$_3$X (X = Ni, Pd, Pt) by the full-potential linearized augmented-plane-wave (FP-LAPW) method.

Therefore, the Ir-based intermetallics with A15 crystal structure should also have the potential to be applied as structural materials. These compounds have been studied for their structural and electronic properties. For instance, Standanmann et al. [16] determined the lattice parameters of A15 X$_3$Ir (X = Ti, V, Cr, Nb and Mo) compounds. Meschel et al. [17] reported the experimental standard enthalpy of formation for V$_3$Ir. Paduani and Kuhnen [18] studied the band structure and Fermi surface of V$_3$Ir using the FP-LAPW method, and discussed Knight shift behavior in the compound. Paduani et al. [19] reported the electronic properties of Nb$_3$Ir via FP-LAPW calculations. Nevertheless, to our knowledge, the elastic and thermodynamic properties of X$_3$Ir (X = Ti, V, Cr, Nb and Mo) intermetallics have rarely been discussed.

This research is divided into the following parts. In the second section, the computational methods of X$_3$Ir (X = Ti, V, Cr, Nb and Mo) intermetallics are offered in detail. In the third section, the results and discussions are presented and discussed based on the effects of refractory metals on the physical and thermodynamic properties of X$_3$Ir compounds, including structural properties, elastic propertie, anisotropic behaviors, anisotropic sound velocities, Debye temperatures, and electronic structures. In the fourth section, the conclusions are drawn and presented in detail.

2. Materials and Methods

The first-principles calculations were performed using the CASTEP code, which is based on the pseudopotential plane-wave within density functional theory [20,21]. Using the ultrasoft pseudopotential [22] to model the ion-electron exchange-correlation, both the generalized gradient approximation (GGA) with the function proposed by Perdew, Burke and Ernzer (PBE) [23,24] and the local density approximation (LDA) with Ceperley–Alder form [25] were used. Additionally, the basis atom states were set as: Ti$3s^33p^63d^35s^2$, V$3s^23p^63d^35s^2$, Cr$3s^23p^63d^54s^1$, Nb$4s^24p^64d^45s^1$, Mo$4s^24p^64d^55s^1$ and Ir$5d^76s^2$. Through a series of tests, the cutoff energy of 400 eV was determined. In addition, a $10 \times 10 \times 10$ k-point mesh in the Brillouin zone was set for the special points sampling integration for the intermetallics. Both lattice constants and atom coordinates should be optimized via minimizing the total energy. Furthermore, the Brodyden–Fletcher–Goldfarb–Shanno (BFGS) minimization scheme was used for the geometric optimization [26,27]. Overall, the maximum stress has to be within 0.02 GPa, the maximum ionic force has to be within 0.01 eV/Å, the maximum ionic displacement has to be within 5.0×10^{-4} Å and the difference of the total energy has to be within 5.0×10^{-6} eV/atom for the geometrical optimization. Finally, the total energy and electronic structure were calculated, followed by cell optimization with a self-consistent field tolerance (5.0×10^{-7} eV/atom). Using the corrected tetrahedron Blöchl method, the total energies at equilibrium structures were derived [28].

3. Results

3.1. Structural Properties

The X_3Ir (X = Ti, V, Cr, Nb and Mo) intermetallics have a A15 cubic structure with the *cP*8 (No. 223) space group. In a unit cell, six X atoms and two Ir atoms are dominated at the sites of 6c (0.25, 0, 0.5) and 2a (0, 0, 0), respectively. For the sake of performing structural property optimizations on IrX$_3$ compounds, the GGA method as well as the LDA method were utilized. The results are exhibited in Table 1, showing that the derived lattice constants using both methods are close to the experimental values [29–33].

Table 1. The optimized and experimental lattice parameters, the calculated deviations and densities for X_3Ir (X = Ti, V, Cr, Nb and Mo) compounds.

Compounds	a_0 (Å)	a_{exp} (Å)	Calculated Deviation (%)	Density (g/cm^3)
Ti$_3$Ir	5.010 [a]	5.012 [c]	−0.041 [a]	8.872 [a]
	4.901 [b]		−2.223 [b]	9.479 [b]
V$_3$Ir	4.7842 [a]	4.7876 [d]	−0.072 [a]	10.463 [a]
	4.6913 [b]		−2.012 [b]	11.099 [b]
Cr$_3$Ir	4.652 [a]	4.685 [e]	−0.712 [a]	11.489 [a]
	4.651 [b]		−0.732 [b]	11.496 [b]
Nb$_3$Ir	5.1585 [a]	5.135 [f]	0.457 [a]	11.394 [a]
	5.0777 [b]		−1.116 [b]	11.946 [b]
Mo$_3$Ir	4.9874 [a]	4.9703 [g]	0.344 [a]	12.986 [a]
	4.9199 [b]		−1.014 [b]	13.387 [b]

[a]: From the GGA method in this work: Theoretical values. [b]: From the LDA method in this work: Theoretical values. [c]: From Reference [29]: Experimental values. [d]: From Reference [30]: Experimental values. [e]: From Reference [31]: Experimental values. [f]: From Reference [32]: Experimental values. [g]: From Reference [33]: Experimental values.

In most compounds, the lattice constants generated by the GGA method offer much smaller calculated deviations than the LDA method (Table 1). For instance, the a_0(GGA) has the calculated deviation of −0.041%, and a_0(LDA) has the calculated deviation of −2.223% in comparison with a_{exp} in Ti$_3$Ir. Clearly, the GGA method exhibited better reliability for structural optimization, and thus giving a superior quality of calculation over the LDA method. As a result, the following calculation work was accomplished only by GGA method.

3.2. Elastic Constants

In the crystalline materials, the elastic constant represented the capability of resisting the exterior imposed stress. In such manners, a whole package of elastic constants was achieved to characterize mechanical properties of crystals. By imposing small strains to the equilibrium unit cell, elastic constants can be computed by determining the corresponding variations in the total energy. Theoretically, the elastic strain energy was formulated by Equation (1):

$$U = \frac{\Delta E}{V_0} = \frac{1}{2}\sum_i^6 \sum_j^6 C_{ij}e_i e_j \tag{1}$$

where V_0 represents the cell volume at equilibrium state; ΔE represents the energy difference; e_i and e_j represent the strains; C_{ij} (*ij* = 1, 2, 3, 4, 5 and 6) represent the elastic constants.

In cubic structures, C_{11}, C_{12} and C_{44} are nonzero elastic constants without mutual dependence. In Table 2, the calculated elastic constants (C_{ij}) for X_3Ir intermetallics are shown, accompanied by the available theoretical values [18,34–36] for comparison.

Table 2. The elastic constant (C_{ij}), Cauthy pressure (C_{12}-C_{44}), bulk modulus (B), shear modulus (G), Young's modulus (E), Poisson's ratio (v) and B/G ratio for X_3Ir (X = Ti, V, Cr, Nb and Mo) intermetallics.

Compounds	C_{ij}			$C_{12}-C_{44}$ (GPa)	B (GPa)	G (GPa)	E (GPa)	v	B/G
	C_{11} (GPa)	C_{44} (GPa)	C_{12} (GPa)						
Ti_3Ir	183.8	52.8	166.0	114.2	171.9	26.5	75.7	0.427	6.483
	207.2 [a]	48.8 [a]	153.1 [a]	104.3 [a]	171.1 [a]	38.5 [a]	107.4 [a]	0.395 [a]	4.446 [a]
V_3Ir	471.5	109.4	136.8	27.4	248.4	129.8	331.7	0.277	1.913
					279.89 [b]				
Cr_3Ir	478.6	89.6	190.2	100.4	286.3	108.5	289.0	0.332	2.639
Nb_3Ir	433.7	84.5	123.7	39.2	227.0	108.0	279.7	0.295	2.102
					216.4 [c]				
Mo_3Ir	512.7	87.6	175.8	88.2	288.1	114.2	302.6	0.325	2.523
					297.5 [d]				

[a]: From Reference [34]: Theoretical values. [b]: From Reference [18]: Theoretical values. [c]: From Reference [35]: Theoretical values. [d]: From Reference [36]: Theoretical values.

In the elastic constant, a larger C_{44} corresponds to a stronger resistance to monoclinic shear in the (100) plane, and therefore symbolizes a larger shear modulus. For instance, V_3Ir has the largest C_{44} and shear modulus, exhibiting a superior capability to resist the shear stress. Furthermore, the compressive resistance along the *x* axis is reflected by C_{11}. For each compound, the derived C_{11} exhibited the biggest value among elastic constants, suggesting that is has the greatest incompressibility under *x* uniaxial stress. Among the compounds, Mo_3Ir was the least compressible along the *x* axis because it had the biggest C_{11} (512.7 GPa), and Ti_3Ir was the most compressible owing to its small C_{11} (183.8 GPa)

Utilizing Born's criteria [37,38], the essence of mechanical stability should be evaluated for cubic crystals:

$$C_{11} > 0; C_{44} > 0; C_{11} - C_{12} > 0; C_{11} + 2 C_{12} > 0 \tag{2}$$

Using the values in Table 2, all X_3Ir compounds were found to have mechanical stability by satisfying the Born's criteria at the ground state.

The Cauchy pressure, illustrated as (C_{12}–C_{44}) [39], should be an effective indicator to evaluate the ductile/brittle nature of cubic crystals. In Pettifor's work [40], a more positive Cauchy pressure symbolized better ductility in the compound [41]. In Table 2, the Cauchy pressures for X_3Ir compounds were all positive in the order of $V_3Ir < Nb_3Ir < Mo_3Ir < Cr_3Ir < Ti_3Ir$, which means that X_3Ir compounds are naturally ductile. Such a result is in good compliance with the Cauchy pressure of Ti_3Ir provided by Rajagopalan [34]. Similarly, other A15 cubic crystals (i.e., V_3X (X = Si and Ge) [13], Nb_3X (X = Al, Ge, Si and Sn) [10] and Nb_3X (X = Al, Ga, In, Sn and Sb) [42]) have ductile characters owing to their positive Cauchy pressures.

3.3. Elastic Properties

Once the elastic constants were achieved, the elastic moduli (i.e., bulk modulus (*B*) and shear modulus (*G*)) could be computed by means of the Voigt–Reuss–Hill (VRH) method [43]. In cubic structures, the equations are exhibited as [44–46]:

$$B_V = B_R = \frac{1}{3}(C_{11} + 2C_{12}) \tag{3a}$$

$$G_V = \frac{1}{5}(C_{11} - C_{12} + 3C_{44}) \tag{3b}$$

$$G_R = \frac{5(C_{11} - C_{12})C_{44}}{4C_{44} + 3(C_{11} - C_{12})} \tag{3c}$$

$$B = \frac{B_V + B_G}{2} \tag{3d}$$

$$G = \frac{G_V + G_G}{2} \tag{3e}$$

When the elastic moduli are achieved, the Young's modulus (*E*) and Poisson's ratio (ν) should be calculated in the second step [47]:

$$E = \frac{9BG}{3B + G} \tag{3f}$$

$$\nu = \frac{3B - 2G}{2(3B + G)} \tag{3g}$$

Lastly, the computed elastic moduli for X_3Ir compounds using the VRH method are tabulated in Table 2 in combination with the available theoretical results for comparison [18,34–36]. Comparably, our calculated bulk moduli showed satisfactory agreement with the theoretical values for Ti_3Ir [34], Nb_3Ir [35] and Mo_3Ir [36], and a value slightly smaller smaller than the theoretical one for V_3Ir [18].

Analytically, the resisting capability against volume fluctuation under pressure is determined by the bulk modulus. For X_3Ir (X = Ti, V, Cr, Nb and Mo) intermetallics, the bulk moduli showed the sequence of $Ti_3Ir < Nb_3Ir < V_3Ir < Cr_3Ir < Mo_3Ir$. In References [48,49], a larger equilibrium cell volume was reported to correspond to a lower bulk modulus in the cubic crystal. Observably, such a conclusion is effective when the alloying elements are in the same cycle of the periodic table of elements (Figure 1a). For example, the bulk moduli are improved in the order of $Ti_3Ir < V_3Ir < Cr_3Ir$ depending on the reduced equilibrium cell volume. Similarly, the bulk modulus of Nb3Ir is smaller than that of Mo_3Ir with the larger equilibrium cell volume of Nb_3Ir (Figure 1a). Nevertheless, when the alloying elements are in the same group of the periodic table, the conclusion is valid for $Nb_3Ir < V_3Ir$, but ineffective for $Cr_3Ir < Mo_3Ir$, where Mo_3Ir actually has a larger equilibrium cell volume.
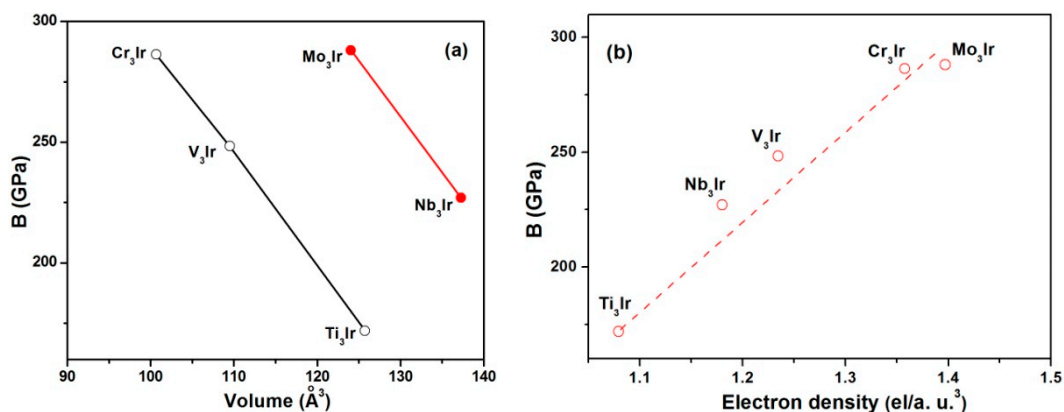

Figure 1. The relationship between bulk modulus and (**a**) volume of the unit cell or (**b**) electron density.

In order to further illustrate the relationship between the equilibrium cell volume and the bulk modulus of X_3Ir intermetallics, the linear dependence of the electron density on the bulk modulus is exhibited in Figure 1b. Clearly, dividing the bonding valence (ZB) by the volume per atom (VM) can deduce the electron density (n) in metallic compounds [50]. For X_3Ir compounds, the electron density (n) can be formulated as:

$$n(X_3Ir) = Z_B(X_3Ir)/V_M(X_3Ir) \tag{4a}$$

where VM(X_3Ir) represents the volume (cm^3/mol) of X_3Ir.

Rationalized by Vegard's law [51], ZB(X_3Ir) showed a bonding valence in (el/atom), and the Reference [52] tabulated the bonding valence of the pure element:

$$Z_B(X_3Ir) = (3Z_B(X) + Z_B(Ir))/4 \tag{4b}$$

Using this method, the linear dependence of the electron density on the bulk modulus was identified through the calculated values. Conclusively, it is more precise to rationalize the bulk modulus from the electron density, rather than the equilibrium cell volume.

Shear modulus (G) symbolizes the capability to resist shape fluctuation [44], and Young's modulus (E) is a measurement of resistance to tension and compression in the elastic regime [53]. Notably, there is a linear dependence of the Young's modulus on the shear modulus following the order of $Ti_3Ir < Nb_3Ir < Cr_3Ir < Mo_3Ir < V_3Ir$ (Figure 2).
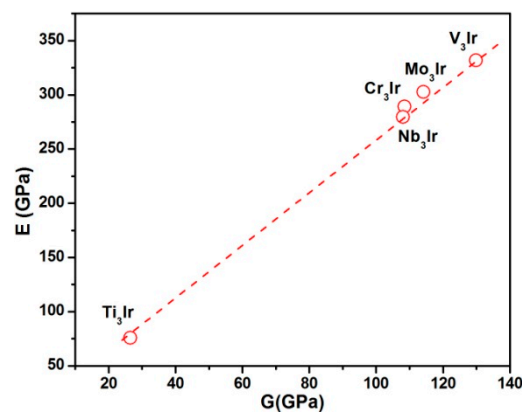

Figure 2. The relationship between shear modulus (G) and Young's modulus (E).

Overall, the bigger bulk modulus over shear modulus for each X_3Ir compound should reflect that the X_3Ir compound has an improved capability to resist volume fluctuation over shape fluctuation (Table 2). This conclusion complies well with the available data regarding the dependence of the bulk modulus on the shear modulus in other A15 intermetallics, i.e., Ti_3Ir (X = Ir, Pt and Au) [34], V_3X (X = Si and Ge) [13], Nb_3X (X = Al, Ga, In, Sn and Sb) [42] and Mo_3X (X = Si and Ge) [54].

The Poisson's ratio ($-1 \leq v \leq 0.5$) is used to quantify the stability of crystals against the shear deformation [55]. Materials with improved plasticity should possess a larger Poisson's ratio. The X_3Ir compounds have Poisson's ratios in the order of $V_3Ir < Nb_3Ir < Mo_3Ir < Cr_3Ir < Ti_3Ir$. This means that Ti_3Ir should be the most ductile, while V_3Ir is most brittle. Additionally, the Poisson's ratio provides information on the bonding forces in solids [56]. The lower and higher limits are 0.25 and 0.5 for the central force in a solid, respectively. For XIr_3 intermetallics, the interatomic forces of intermetallics should be central forces, since all the obtained values are located on this scale (Table 2).

The B/G ratio formulated by Pugh [57] is commonly adopted to quantitatively estimate the brittle or ductile essence of metallic compounds. The critical B/G ratio to distinguish the brittle from ductile material is 1.75. A smaller value is connected with the brittle nature, whereas a larger B/G ratio is related to ductility. Furthermore, the revised Cauchy pressure ($(C_{12}-C_{44})/E$) [58] was plotted against the B/G ratio to clarify the extent of ductility intuitively (Figure 3). As a result, the ductility was found to be enhanced in the order of $V_3Ir < Nb_3Ir < Mo_3Ir < Cr_3Ir < Ti_3Ir$. This conclusion agrees well with the analysis of the Poisson's ratio. Clearly, Ti_3Ir should be much more ductile than the other X_3Ir compounds (Figure 3).
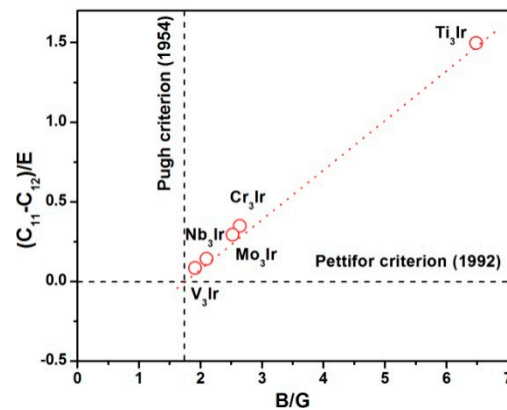
Figure 3. Revised Cauchy pressure $(C_{12}-C_{44})/E$ as a factor of the B/G ratio for X_3Ir compounds.

3.4. Elastic Anisotropy

The universal anisotropic index (A^U) can be used to evaluate the elastic anisotropy, which is also referred to as the probability to introduce materials' micro-cracks [59]. The index can be calculated via Equation (5) [60]:

$$A^U = 5\frac{G_V}{G_R} + \frac{B_V}{B_R} - 6 \tag{5}$$

where B_V (B_R) and G_V (G_R) represent the symbols of the bulk modulus and the shear modulus at Voigt (Reuss) bounds, respectively.

In the calculated elastic anisotropies, B_V/B_R, should be equal to 1 for cubic crystals (Table 3).

Table 3. The computed bulk and shear moduli at Voigt (Reuss) bounds, and the universal anisotropic index (A^U) for X_3Ir compounds.

Compounds	B_V	B_R	G_V	G_R	B_V/B_R	G_V/G_R	A^U
Ti_3Ir	171.9	171.9	35.3	17.8	1	1.984	4.922
V_3Ir	248.4	248.4	132.6	127.0	1	1.044	0.220
Cr_3Ir	286.3	286.3	111.4	105.6	1	1.055	0.277
Nb_3Ir	227.0	227.0	112.7	103.3	1	1.091	0.455
Mo_3Ir	288.1	288.1	119.9	108.4	1	1.106	0.532

Indeed, G_V/G_R has a decisive effect on the universal anisotropic index (A^U). Figure 4 shows that the universal anisotropic index increases linearly with the increment of the G_V/G_R value. A compound with a smaller A^U represents a weaker extent of anisotropy. Therefore, the universal anisotropy was found to be reduced in the sequence of $V_3Ir < Cr_3Ir < Nb_3Ir < Mo_3Ir < Ti_3Ir$. Generally, Ti_3Ir has the largest universal anisotropy, and V_3Ir has the smallest. Because the experimental value is lacking for comparison in these compounds, this calculation has to be evaluated in later research.

In addition, to further describe the anisotropy of X_3Ir compounds, the directional dependence of the reciprocal of the Young's modulus was constructed for a three-dimensional (3D) surface according to Equation (6) [48]:

$$\frac{1}{E} = S_{11} - 2(S_{11} - S_{12} - \frac{S_{44}}{2})(l_1^2 l_2^2 + l_2^2 l_3^2 + l_1^2 l_3^2) \tag{6}$$

where S_{ij} represents the usual elastic compliance constant obtained from the inverse of the matrix of the elastic constant; l_1, l_2 and l_3 represent the direction cosines in the sphere coordination.

If a crystal has ideal isotropic performance, the 3D directional dependence of the Young's modulus would show a spherical shape. In fact, the extent of deviation from the spherical shape symbolizes the anisotropic extent. In Figure 5, X_3Ir compounds showed the distinctive 3D figures of Young's moduli

with various deviations from a sphere. This confirmed that X_3Ir compounds have anisotropic behaviors. Obviously, Ti_3Ir shows the largest deviation from the sphere shape along the <111> direction. On the contrary, other X_3Ir compounds exhibited different forms of deviation, and the most visible deviations were observed along the zone axes. Finally, the extent of the elastic anisotropy for X_3Ir obeyed the sequence of $V_3Ir < Cr_3Ir < Nb_3Ir < Mo_3Ir < Ti_3Ir$. This conclusion complies well with the result obtained from the universal anisotropic index.
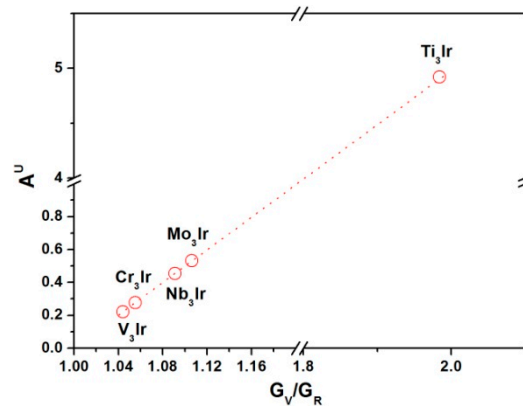

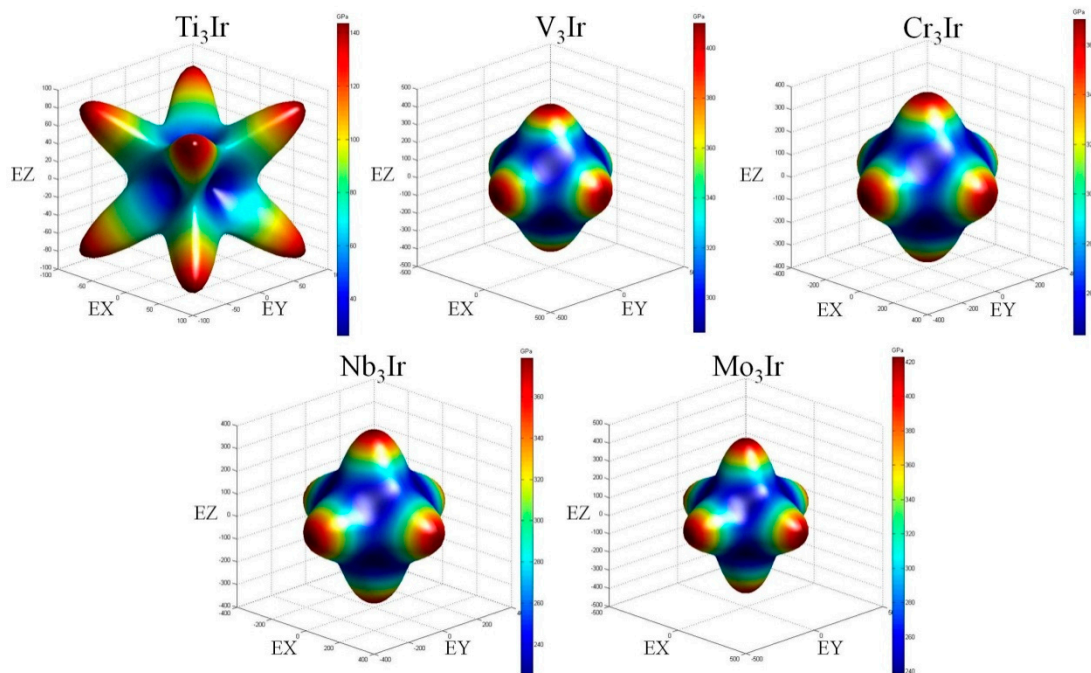**Figure 4.** The correlation between G_V/G_R and the universal anisotropic index (A^U).

Figure 5. The 3D surface construction of the Young's modulus in X_3Ir compounds. (The magnitudes of Young's moduli at different directions are presented by the contours along each graph with the unit of GPa).

3.5. Anisotropic Sound Velocity and Debye Temperature

In the crystalline material, the sound velocities should depend on the crystalline symmetry in combination with the propagating direction. In the cubic structure, [111], [110] and [001] directions exhibited the pure transverse and longitudinal modes, accordingly. Regarding other directions, both

quasi-transverse and quasi-longitudinal waves can work as the main sound propagating modes. Therefore, the sound velocities formulated in the principal directions are listed as follows [61]:

$$[100]v_l = \sqrt{C_{11}/\rho}; [010]v_{t1} = [001]v_{t2} = \sqrt{C_{44}/\rho}$$
$$[110]v_l = \sqrt{(C_{11} + C_{12} + C_{44})/(2\rho)}$$
$$[1\bar{1}0]v_{t1} = \sqrt{(C_{11} - C_{12})/\rho}; [001]v_{t2} = \sqrt{C_{44}/\rho} \qquad (7)$$
$$[111]v_l = \sqrt{(C_{11} + 2C_{12} + 4C_{44})/(3\rho)}$$
$$[11\bar{2}]v_{t1} = [11\bar{2}]v_{t2} = \sqrt{(C_{11} - C_{12} + C_{44})/(3\rho)}$$

where v_l (v_t) represents the longitudinal (transverse) sound velocity; ρ represents the density (see Table 1).

Overall, the longitudinal sound velocity along the [100] direction was only decided by C_{11}. The transverse modes along [010] and [001] directions were dependent on C_{44}. The longitudinal sound velocities along both the [110] and [111] directions were influenced by C_{11}, C_{12} and C_{44}.

Along the [100], [110] and [111] directions, the longitudinal sound velocities and the transverse sound velocities are exhibited in Table 4 for each X_3Ir compound. For each compound, the longitudinal sound velocity followed the rising sequence of [100] < [110] < [111]. The sound velocities showed anisotropic properties, further confirming the elastic anisotropic behaviors of the compounds.

These theoretically computed physical properties (i.e., elastic moduli and Poisson's ratio) and structural properties (i.e., density) should be adopted to calculate the Debye temperature (Θ) using the following formula [54,62,63]:

$$\Theta = \frac{h}{k} \left[\frac{3n}{4\pi} \left(\frac{N_A \rho}{M} \right) \right]^{\frac{1}{3}} V_D \qquad (8a)$$

where ρ represents the density (see Table 1); h represents the Planck's constant ($h = 6.626 \times 10^{-34}$ J/s); k represents the Boltzmann's constant ($k = 1.381 \times 10^{-23}$ J/K); n represents the number of atoms per formula unit; N_A represents the Avogadro's number ($N_A = 6.023 \times 10^{-23}$/mol); M represents the molecular weight (M(Ti$_3$Ir) = 335.8 g/mol, M(V$_3$Ir) = 345 g/mol, M(Cr$_3$Ir) = 347.8 g/mol, M(Nb$_3$Ir) = 470.9 g/mol, M(Mo$_3$Ir) = 480 g/mol); v_D represents the average sound velocity in polycrystalline materials. The latter is formulated as:

$$v_D = \left[\frac{1}{3} \left(\frac{1}{V_L^3} + \frac{2}{V_T^3} \right) \right]^{-\frac{1}{3}} \qquad (8b)$$

where v_T and v_L represent the transverse and longitudinal sound velocities, respectively, as formulated by the equations below:

$$v_T = \sqrt{\frac{G}{\rho}} \qquad (8c)$$

$$v_L = \sqrt{\frac{B + \frac{4}{3}G}{\rho}} \qquad (8d)$$

Table 4. The anisotropic sound velocities (m/s), average sound velocities (m/s) and Debye temperatures (K) for X_3Ir intermetallics.

Crystalline Orientation		Ti₃Ir	V₃Ir	Cr₃Ir	Nb₃Ir	Mo₃Ir
[111]	$[111]v_l$	5226.6	6138.7	5942.8	5460.3	5583.6
	$[11\bar{2}]v_{t1,2}$	1629.2	3762.0	3311.6	3397.4	3301.0
[110]	$[110]v_l$	4763.3	5856.6	5744.8	5307.3	5466.2
	$[1\bar{1}0]v_{t1}$	1416.9	5656.7	5010.3	5216.1	5093.6
	$[001]v_{t2}$	2440.3	3234.2	2792.4	2723.7	2597.2
[100]	$[100]v_l$	4551.4	6713.4	6454.1	6169.4	6283.3
	$[010]v_{t1}$	2440.3	3234.2	2792.4	2723.7	2597.2
	$[001]v_{t2}$	2440.3	3234.2	2792.4	2723.7	2597.2
	v_L	4833.4	6346.8	6124.7	5706.4	5822.9
	v_T	1728.8	3522.6	3073.2	3079.0	2965.2
	v_D	1962.7	3920.4	3444.0	3434.1	3320.0
	Θ	233.3 238 [a], 262.6 [b]	487.9 460 ± 10 [c], 445 [d]	441.0 449 [e]	396.4 409 ± 8 [c], 377 [d]	397.8 452 [f], 325 [g], 497.06 [h]

[a]: From Reference [64]: Experimental values. [b]: From Reference [34]: Theoretical values. [c]: From Reference [65]: Experimental values. [d]: From Reference [66]: Experimental values. [e]: From Reference [67]: Experimental values. [f]: From Reference [16]: Experimental values. [g]: From Reference [68]: Experimental values. [h]: From Reference [36]: Theoretical values.

For each X_3Ir compound, the derived Debye temperature (Θ) is tabulated in Table 4. Also, the published experimental [16,64–68] and theoretical [34,36] values are included for comparison.

Generally, V_3Ir had the largest Debye temperature, and Ti_3Ir had the smallest. The calculated Debye temperatures were in the order of $Ti_3Ir < Nb_3Ir < Mo_3Ir < Cr_3Ir < V_3Ir$. Clearly, our results revealed the reduced tendency of Debye temperatures with the M atom in the same group, i.e., Cr (Lighter element) and Mo (Heavier element) are from Group-VIB, and V (Lighter element) and Nb (Heavier element) are from Group-VB.

Comparably, the obtained Debye temperatures for Ti_3Ir, V_3Ir, Cr_3Ir and Nb_3Ir were all in excellent agreement with the available experimental results [16,64–68]. For instance, the calculated Θ was 233 K for Ti_3Ir. This agrees well with the experimental values reported by Junod et al. [64] with the calculated deviation of 2.01%. Notably, the Debye temperature reported by Rajagopalan et al. [34] had the calculated deviation of 10.3%, indicating the poor quality of the prediction in this work. However, for Mo_3Ir, the published experimental [16,68] and theoretical [36] Debye temperatures were quite scattered, although our calculated values were closer to the experimental values from Staudenmann's report [16]. Nevertheless, more works are required on this compound.

Because both structural parameters and elastic moduli are incorporated to calculate the Debye temperature, the superior quality of our calculation on these structural and elastic parameters using the GGA method was evidenced by the smaller differences between the estimated and experimental values of Debye temperatures.

3.6. Electronic Structures

Figure 6a–e exhibit the density of states (DOS) spectra representing the calculated electronic structures for X_3Ir compounds. The DOS spectra for these A15 cubic phases were similar to each other. In a typical DOS spectrum, there are normally three regions, including the lower electron band, the upper electron band, and the conduction unoccupied states around the Fermi level (E_F). For example (Figure 6a), the lower the electron band was mainly contributed by 4*s* electrons of Ti ranging from −55 to −57.5 eV. The upper electron band was occupied by 3*p* electrons of Ti ranging from −32 to −35 eV. Around the Fermi level, the conduction unoccupied states were created through the hybridization of mainly Ti3*d* electrons with Ti3*p*, Ir5*d* and Ir4*p* electrons. X_3Ir compounds were plotted around the

Fermi level at zero in all the total DOS (TDOS) and partial DOS (PDOS) spectra. Clearly, no any energy gap can be found near the Fermi level. Therefore, their nature of metallicity was confirmed.
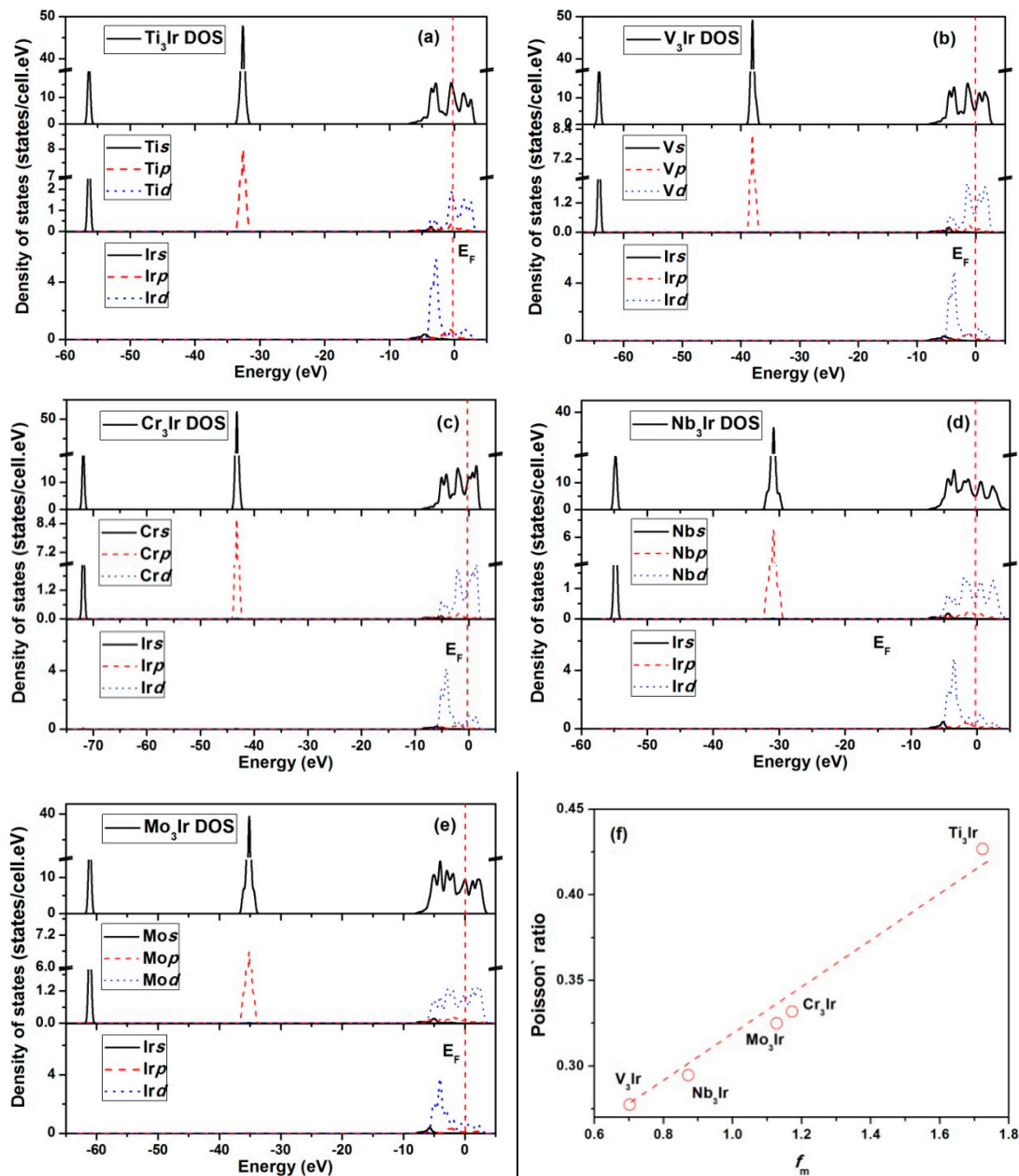

Figure 6. Total density of states (TDOS) and partial density of states (PDOS) spectra for (**a**) Ti_3Ir, (**b**) Cr_3Ir, (**c**) Mo_3Ir, (**d**) Nb_3Ir and (**e**) V_3Ir; (**f**) the correlation between metallicity and the Poisson's ratio in X_3Ir compounds.

Furthermore, the electron density values can provide quantitative evidence of the metallic nature in the bonding characteristics. Even at the Fermi surface, the electron density values were much larger than zero. According to the electronic Fermi liquid theory [69], the metallicity of the compound has to be estimated using Equation (9) [70]:

$$f_m = \frac{n_m}{n_e} = \frac{k_B T D_f}{n_e} = \frac{0.026 D_f}{n_e} \qquad (9)$$

where

k_B represents the Boltzmann constant ($k = 1.381 \times 10^{-23}$ J/K);

T represents the absolute temperature;

D_f represents the DOS value at the Fermi level;

n_m and n_e represent the thermally excited electrons and valence electron density of the cell, respectively;

n_e is calculated by $n_e = N/V_{cell}$ (N represents the total number of valence electrons; V_{cell} represents the cell volume).

Using the calculated metallicity values (f_m), the correlation between metallicity and Poisson's ratios can be constructed for X_3Ir compounds (Figure 6f). It was found that the Poisson's ratios were diminished with the reduction in metallicity in compounds with the order of $V_3Ir < Nb_3Ir < Mo_3Ir < Cr_3Ir < Ti_3Ir$. This indicated that a compound with higher metallicity in its bonds should possess better ductility.

4. Conclusions

The effects of refractory metals on physical and thermodynamic properties of X_3Ir (X = Ti, V, Cr, Nb and Mo) intermetallics were investigated utilizing first-principles calculations. The conclusions are listed as follows:

(1) Using the GGA method to structurally optimized the unit cell, smaller calculation deviations for lattice constants were achieved as compared to those achieved using the LDA method.

(2) The calculated bulk moduli exhibited the increasing sequence of $Ti_3Ir < Nb_3Ir < V_3Ir < Cr_3Ir < Mo_3Ir$. Furthermore, the bulk moduli showed a linear relationship with electron densities. The Young's modulus showed a linear dependence on shear modulus following the order of $Ti_3Ir < Nb_3Ir < Cr_3Ir < Mo_3Ir < V_3Ir$.

(3) Based on the discussions on the Cauchy pressure, Poisson's ratio and *B/G* ratio, the ductile essence was found to be enhanced in the order of $V_3Ir < Nb_3Ir < Mo_3Ir < Cr_3Ir < Ti_3Ir$.

(4) For X_3Ir compounds, the extent of the elastic anisotropy for X_3Ir obeyed the increasing sequence of $V_3Ir < Cr_3Ir < Nb_3Ir < Mo_3Ir < Ti_3Ir$ via the analyses of the universal anisotropic indexes and 3D surface constructions.

(5) The Debye temperatures obtained for Ti_3Ir, V_3Ir, Cr_3Ir and Nb_3Ir were all in good agreement with the results from experiments. Such good compliance proved the superior quality of our calculations of the structural and elastic properties, since the computation of Debye temperature is concerned with both structural and elastic parameters.

(6) The calculated electronic structures for X_3Ir compounds showed similar features in the DOS spectra. Furthermore, the metallicity of the compounds was calculated, and was correlated with the Poisson's ratios. This indicated that a compound with higher metallicity in its bonds should possess better ductility.

References and Notes

1. Yamaguchi, M.; Inui, H.; Ito, K. High-temperature structural intermetallics. *Acta Mater.* **2000**, *48*, 307–322. [CrossRef]
2. Yu, X.; Yamabe-Mitarai, Y.; Ro, Y.; Harada, H. New developed quaternary refractory superalloys. *Intemetallics* **2000**, *8*, 619–622. [CrossRef]
3. Yamabe-Mitarai, Y.; Gu, Y.; Huang, C.; Völkl, R.; Harada, H. Platinum-group-metal-based intermetallics as high-temperature structural materials. *JOM* **2004**, *56*, 34–39. [CrossRef]
4. Yamabe-Mitari, Y.; Ro, Y.; Maruko, T.; Harada, H. Microstructure dependence of strength of Ir-base refractory superalloys. *Intermetallics* **1999**, *7*, 49–58. [CrossRef]
5. Yamabe-Mitarai, Y.; Ro, Y.; Nakazawa, S. Temperature dependence of the flow stress of Ir-based L1$_2$ intermetallics. *Intermetallics* **2001**, *9*, 423–429. [CrossRef]
6. Terada, Y.; Ohkubo, K.; Miura, S.; Sanchez, J.M.; Mohri, T. Thermal conductivity and thermal expansion of Ir$_3$X (X = Ti, Zr, Hf, V, Nb, Ta) compounds for high-temperature applications. *Mater. Chem. Phys.* **2003**, *80*, 385–390. [CrossRef]
7. Chen, K.; Zhao, L.R.; Tse, J.S. Ab initio study of elastic properties of Ir and Ir$_3$X compounds. *J. Appl. Phys.* **2003**, *93*, 2414–2417. [CrossRef]
8. Liu, N.; Wang, X.; Wan, Y. Firstprinciple calculations of elastic and thermodynamic properties of Ir3Nb and Ir3V with L12 structure under high pressure. *Intermetallics* **2015**, *66*, 103–110. [CrossRef]
9. Pan, Y.; Lin, Y.; Xue, Q.; Ren, C.; Wang, H. Relationship between Si concentration and mechanical properties of Nb-Si compounds: A first-principles study. *Mater. Des.* **2016**, *89*, 676–683. [CrossRef]
10. Papadimitriou, I.; Utton, C.; Scott, A.; Tsakiropoulos, P. Ab Initio Study of Binary and Ternary Nb$_3$(X,Y) A15 Intermetallic Phases (X,Y = Al, Ge, Si, Sn). *Metall. Mater. Trans. A* **2015**, *46*, 566–576. [CrossRef]
11. Papadimitriou, I.; Utton, C.; Tsakiropoulos, P. Ab initio investigation of the intermetallics in the Nb-Sn binary system. *Acta Mater.* **2015**, *86*, 23–33. [CrossRef]
12. Papadimitriou, I.; Utton, C.; Tsakiropoulos, P. Ab initio investigation of the Nb-Al system. *Comput. Mater. Sci.* **2015**, *107*, 116–121. [CrossRef]
13. Chihi, T.; Fatmi, M. Theoretical prediction of the structural, elastic, electronic and thermodynamic properties of V$_3$M (M = Si, Ge and Sn) compounds. *Superlatt. Microstruc.* **2012**, *52*, 697–703. [CrossRef]
14. Jarlborg, T.; Junod, A.; Peter, M. Electronic structure, superconductivity, and spin fluctuations in the A15 compounds A$_3$B: A =V, Nb; B=Ir, Pt, Au. *Phys. Rev. B* **1983**, *27*, 1558–1567. [CrossRef]
15. Paduani, C.; Kuhnen, C.A. Band structure calculations in isoelectronic V3B compounds: B=Ni, Pd and Pt. *Solid State Commun.* **2010**, *150*, 1303–1307. [CrossRef]
16. Staudenmann, J.L.; DeFacio, B.; Testardi, L.R.; Werner, S.A.; Flükiger, R.; Muller, J. Debye classes in A15 compounds. *Phys. Rev. B* **1981**, *24*, 6446. [CrossRef]
17. Meschel, S.V.; Kleppa, O.J. The standard enthalpies of formation of some intermetallic compounds of transition metals by high temperature direct synthesis calorimetry. *J. Alloy. Compd.* **2006**, *415*, 143–149. [CrossRef]
18. Paduani, C.; Kuhnen, C.A. Electronic structure of A15-type compounds: V$_3$Co, V$_3$Rh, V$_3$Ir and V$_3$Os. *Eur. Phys. J. B* **2009**, *69*, 331–336. [CrossRef]
19. Paduani, C. Electronic properties of the A-15 Nb-based intermetallics Nb3(Os,Ir,Pt,Au). *Solid State Commun.* **2007**, *144*, 352–356. [CrossRef]
20. Segall, M.D.; Lindan, P.J.D.; Probert, M.J.; Pickard, C.J.; Hasnip, P.J.; Clark, S.J.; Payne, M.C. First-principles simulation: Ideas, illustrations and the CASTEP code. *J. Phys. Condens. Matter* **2002**, *14*, 2717–2744. [CrossRef]
21. Clark, S.J.; Segall, M.D.; Pickard, C.J.; Hasnip, P.J.; Probert, M.J.; Refson, K.; Payne, M.C. First principles methods using CASTEP. *Zeitschrift fuer Kristallographie* **2005**, *220*, 567–570. [CrossRef]
22. Vanderbilt, D. Soft self-consistent pseudopotentials in a generalized eigenvalue formalism. *Phys. Rev. B* **1990**, *41*, 7892–7895. [CrossRef]
23. Perdew, J.P.; Wang, Y. Accurate and simple analytic representation of the electron-gas correlation energy. *Phys. Rev. B* **1992**, *45*, 13244–13249. [CrossRef]
24. Perdew, J.P.; Burke, K.; Ernzerhof, M. Generalized Gradient Approximation Made Simple. *Phys. Rev. Lett.* **1996**, *77*, 3865–3868. [CrossRef]

25. Perdew, J.P.; Zunger, A. Self-interaction correction to density-functional approximations for many-electron systems. *Phys. Rev. B* **1981**, *23*, 5048–5079. [CrossRef]

26. Shanno, D.F. Conditioning of quasi-Newton methods for function minimization. *Math. Comput.* **1970**, *24*, 647–656. [CrossRef]

27. Fischer, T.H.; Almlof, J. General Methods for Geometry and Wave Function Optimization. *J. Chem. Phys.* **1992**, *96*, 9768–9774. [CrossRef]

28. Blöchl, P.E.; Jepsen, O.; Andersen, O.K. Improved tetrahedron method for Brillouin-zone integrations. *Phys. Rev. B* **1994**, *49*, 16223–16233. [CrossRef]

29. *Ti$_3$Ir, ICSD No. 641115.*

30. *V$_3$Ir, ICSD No. 104591.*

31. *Cr$_3$Ir, ICSD No. 102780.*

32. *Nb$_3$Ir, ICSD No. 640833.*

33. *Mo$_3$Ir, ICSD No.600761.*

34. Rajagopalan, M.; Gandhi, R.R. First principles study of structural, electronic, mechanical and thermal properties of A15 intermetallic compounds Ti$_3$X (X = Au, Pt, Ir). *Phys. B* **2012**, *407*, 4731–4734. [CrossRef]

35. Paduani, C. Structural and electronic properties of the A-15 compounds Nb$_3$Rh and Nb$_3$Ir. *Phys. B* **2007**, *393*, 105–109. [CrossRef]

36. Subhashree, G.; Sankar, S.; Krithiga, R. Superconducting properties of Mo$_3$Os,Mo$_3$Pt,Mo$_3$Ir from first principle calculations. *Mod. Phys. Lett. B* **2014**, *28*, 1450233. [CrossRef]

37. Afaq, A.; Rizwan, M.; Bakar, A. Computational investigations of XMgGa (X = Li, Na) half Heusler compounds for thermo-elastic and vibrational properties. *Phys. B* **2019**, *554*, 102–106. [CrossRef]

38. Heciri, D.; Belkhir, H.; Belghit, R.; Bouhafs, B.; Khenata, R.; Ahmed, R.; Bouhemadou, A.; Ouahrani, T.; Wang, X.; Omrani, S.B. Insight into the structural, elastic and electronic properties of tetragonal inter-alkali metal chalcogenides CsNaX (X = S, Se, and Te) from first-principles calculations. *Mater. Chem. Phys.* **2019**, *221*, 125–137. [CrossRef]

39. He, D.G.; Lin, Y.C.; Jiang, X.Y.; Yin, L.X.; Wang, L.H.; Wu, Q. Dissolution mechanisms and kinetics of δ phase in an aged Ni-based superalloy in hot deformation process. *Mater. Des.* **2018**, *156*, 262–271. [CrossRef]

40. Pettifor, D.G. Theoretical predictions of structure and related properties of intermetallics. *Mater. Sci. Technol.* **1992**, *8*, 345–349. [CrossRef]

41. Fatima, B.; Chouhan, S.S.; Acharya, N.; Sanyal, S.P. Theoretical prediction of the electronic structure, bonding behavior and elastic moduli of scandium intermetallics. *Intermetallics* **2014**, *53*, 129–139. [CrossRef]

42. Sundareswari, M.; Ramasubramanian, S.; Rajagopalan, M. Elastic and thermodynamical properties of A15 Nb$_3$X (X = Al,Ga,In,Sn and Sb) compounds-First principles DFT study. *Solid State Commun.* **2010**, *150*, 2057–2060. [CrossRef]

43. Han, Y.; Wu, Y.; Li, T.; Khenata, R.; Yang, T.; Wang, X. Electronic, Magnetic, Half-Metallic, and Mechanical Properties of a New Equiatomic Quaternary Heusler Compound YRhTiGe: A First-Principles Study. *Materials* **2018**, *11*, 797. [CrossRef]

44. Chen, D.; Chen, Z.; Wu, Y.; Wang, M.; Ma, N.; Wang, H. First-principles investigation of mechanical, electronic and optical properties of Al$_3$Sc intermetallic compound under pressure. *Comput. Mater. Sci.* **2014**, *91*, 165–172. [CrossRef]

45. Salma, M.U.; Rahman, M.A. Study of structural, elastic, electronic, mechanical, optical and thermodynamic properties of NdPb$_3$ intermetallic compound: DFT based calculations. *Comput. Condens. Matter* **2018**, *15*, 42–47. [CrossRef]

46. Luan, X.; Qin, H.; OrcID, F.L.; Dai, Z.; Yi, Y.; Li, Q. The Mechanical Properties and Elastic Anisotropies of Cubic Ni$_3$Al from First Principles Calculations. *Crystals* **2018**, *8*, 307. [CrossRef]

47. Sultana, F.; Uddin, M.M.; Ali, M.A.; Hossain, M.M.; Naqib, S.H.; Islam, A.K.M.A. First principles study of M$_2$InC (M = Zr, Hf and Ta) MAX phases: The effect of M atomic species. *Results Phys.* **2018**, *11*, 869–876. [CrossRef]

48. Chen, S.; Sun, Y.; Duan, Y.H.; Huang, B.; Peng, M.J. Phase stability, structural and elastic properties of C15-type Laves transition-metal compounds MCo$_2$ from first-principles calculations. *J. Alloy. Compd.* **2015**, *630*, 202–208. [CrossRef]

49. Li, C.X.; Duan, Y.H.; Hu, W.-C. Electronic structure, elastic anisotropy, thermal conductivity and optical properties of calcium apatite Ca$_5$(PO$_4$)$_3$X (X = F, Cl or Br). *J. Alloy. Compd.* **2015**, *619*, 66–77. [CrossRef]

50. Huang, S.; Zhang, C.H.; Li, R.Z.; Shen, J.; Chen, N.X. Site preference and alloying effect on elastic properties of ternary B2 RuAl-based alloys. *Intermetallics* **2014**, *51*, 24–29. [CrossRef]

51. Jacob, K.T.; Raj, S.; Rannesh, L. Vegard's law: A fundamental relation or an approximation? *Inter. J. Mater. Res.* **2007**, *98*, 776–779. [CrossRef]

52. Li, C.; Wu, P. Correlation of Bulk Modulus and the Constituent Element Properties of Binary Intermetallic Compounds. *Chem. Mater.* **2001**, *13*, 4642–4648. [CrossRef]

53. Chen, D.; Chen, Z.; Wu, Y.; Wang, M.; Ma, N.; Wang, H. First-principles study of mechanical and electronic properties of TiB compound under pressure. *Intermetallics* **2014**, *52*, 64–71. [CrossRef]

54. Zhong, S.Y.; Chen, Z.; Wang, M.; Chen, D. Structural, elastic and thermodynamic properties of Mo_3Si and Mo_3Ge. *Eur. Phys. J. B* **2016**, *89*, 6. [CrossRef]

55. Lebga, N.; Daoud, S.; Sun, X.W.; Bioud, N.; Latreche, A. Mechanical and Thermophysical Properties of Cubic Rock-Salt AlN Under High Pressure. *J. Electr. Mater.* **2018**, *47*, 3430–3439. [CrossRef]

56. Fu, H.; Li, D.; Peng, F.; Gao, T.; Cheng, X. Ab initio calculations of elastic constants and thermodynamic properties of NiAl under high pressures. *Comput. Mater. Sci.* **2008**, *44*, 774–778. [CrossRef]

57. Pugh, S.F. XCII. Relations between the elastic moduli and the plastic properties of polycrystalline pure metals. *Philos. Mag.* **1954**, *45*, 823–843. [CrossRef]

58. Niu, H.Y.; Chen, X.Q.; Liu, P.T.; Xing, W.W.; Cheng, X.Y.; Li, D.Z.; Li, Y.Y. Extra-electron induced covalent strengthening and generalization of intrinsic ductile-to-brittle criterion. *Sci. Rep.* **2012**, *2*, 718. [CrossRef]

59. Han, C.; Chai, C.; Fan, Q.; Yang, J.; Yang, Y. Structural, Electronic, and Thermodynamic Properties of Tetragonal t-SixGe3-xN4. *Materials* **2018**, *11*, 397. [CrossRef]

60. Belghit, R.; Belkhir, H.; Kadri, M.T.; Heciri, D.; Bououdin, M.; Ahuja, R. Structural, elastic, electronic and optical properties of novel antiferroelectric KNaX (X = S, Se, and Te) compounds: First principles study. *Phys. B* **2018**, *545*, 18–29. [CrossRef]

61. Duan, Y.H.; Sun, Y.; Peng, M.J.; Zhou, S.G. Anisotropic elastic properties of the Ca-Pb compounds. *J. Alloy. Compd.* **2014**, *595*, 14–21. [CrossRef]

62. Vajeeston, P.; Ravindran, P.; Fjellvag, H. Prediction of structural, lattice dynamical, and mechanical properties of CaB_2. *RSC Adv.* **2012**, *2*, 11687–11694. [CrossRef]

63. Haque, E.; Hossain, M.A. First-principles study of elastic, electronic, thermodynamic, and thermoelectric transport properties of TaCoSn. *Results Phys.* **2018**, *10*, 458–465. [CrossRef]

64. Junod, A.; Flukiger, R.; Muller, J. Supraconductivite et chaleur specifique dans les alliages A15 a base de titane. *J. Phys. Chem. Solids* **1976**, *37*, 27–31. [CrossRef]

65. Spitzli, P. Chaleur spécifique d'alliages de structure A 15. *Physik der kondensierten Materie* **1971**, *13*, 22–58.

66. Junod, A.; Bischel, D.; Muller, J. Eliashberg inversion of superconducting state thermodynamics. *Helv. Phys. Acta* **1979**, *52*, 580. [CrossRef]

67. Flükiger, R.; Heiniger, F.; Junod, A.; Muller, J.; Spitzli, P.; Staudenmann, J.L. Chaleur specifique et supraconductivite dans des alliages de structure A 15 a base de chrome. *J. Phys. Chem. Solids* **1971**, *32*, 459–463. [CrossRef]

68. Morin, F.J.; Maita, J.P. Specific Heats of Transition Metal Superconductors. *Phys. Rev.* **1963**, *129*, 1115. [CrossRef]

69. Misawa, S. The 3-Dimensional Fermi Liquid Description for the Iron-Based Superconductors. *J. Low Temp. Phys.* **2018**, *190*, 45–66. [CrossRef]

70. Li, Y.; Gao, Y.; Xiao, B.; Min, T.; Fan, Z.; Ma, S.; Xu, L. Theoretical study on the stability, elasticity, hardness and electronic structures of W-C binary compounds. *J. Alloy. Compd.* **2010**, *502*, 28–37. [CrossRef]